

# Direct Numerical Simulation of Turbulent Planar Jets with Polymer Additives

Nuno Filipe Cabral Pimentel  
nuno.pimentel@tecnico.ulisboa.pt

Instituto Superior Técnico, Universidade de Lisboa, Portugal

November 2018

## Abstract

In this study it was performed Direct Numerical Simulations (DNS) of a spatial turbulent planar jet with polymer additives to further understand the mechanism of polymer interaction on jet flows. These simulations were achieved with the implementation of the visco-elastic fluid numerical model, represented by the rheological constitutive FENE-P model. The numerical model for the conformation tensor transport equation was adapted for the non-periodic boundary conditions of the flow, for which no references are present in the literature. The development of the numerical algorithm took into consideration the computational performance of the simulations, in which it was implemented a ghost cell mechanism to decrease the computation time. The developed algorithm has been extensively verified to ensure the correct resolution of the governing equations for turbulent jet flow with polymer additives. The numerical model was tested in direct numerical simulation for different polymer molecules physical characteristics, namely the polymeric concentration and the relaxation time. The observed results verified a decrease in the jet width on the presence of a visco-elastic flow, together with a decrease of the viscous energy dissipation rate. It should be noted that the implemented numerical model represents a major progress on the numerical simulations of turbulent spatial jet flow with polymer additives, providing the first numerical results for this kind of study.

**Keywords:** Visco-elastic turbulence, DNS, FENE-P, Spatial turbulent planar jet

## 1. Introduction

Since Toms (1948) [1] reported turbulent drag reduction by the addition of long-chain polymers by up to 80 percent, this effect has been studied for both practical and theoretical purposes. Currently, industrial applications regarding polymer drag reduction are mostly related to long-distance liquid transportation pipeline systems.

This work will focus on the study of this phenomenon on turbulent jet flows, in order to further understand the mechanism of polymer interaction. The framework of this study has potential applications on the aerospace industry, namely on heat transfer reduction by injection of micro-jets into turbine blades [2]. There is a potential application on combining viscoelastic fluids with the micro-jet structures, as the heat transfer behavior of viscoelastic fluids has been studied recently, namely focused on cooling applications for turbine disks [3].

Moreover, it is possible to make a formal analogy between the Finite Extensible Nonlinear Elastic - Peterlin (FENE-P) set of equations for viscoelastic flows and magneto-hydrodynamics (MHD) equations, as mentioned in [4]. Thus the numeri-

cal model considered here to simulate polymer solutions (FENE-P) will have a strong resemblance and application to the methodology used in numerical simulations of MHD flows. As for aerospace industry applications, in recent years plasma flows have rapidly become an important set of new technologies that find application to hypersonic propulsion, being evident a growing interest in plasma-based flow manipulation through MHD forces [5].

## 2. Background

Turbulence is a characteristic of the flow, being generally associated with flows that are highly unsteady with chaotic variations of velocity and pressure in space and time.

The concept of energy transfer through scales in turbulence was translated into a quantitative theory by Kormogorov for a Newtonian fluid. For the case of a visco-elastic fluid, the polymer interaction with the flow leads to a steepening of the kinetic energy spectrum beyond a wavenumber  $l_p$ , which is the Lumley length-scale. In [6], it is presented a model spectrum for the visco-elastic fluid (supported by experimental results) consisting on 3 major regions: (I) Inertial cascade, (E) Elastic subrange and (V)

Viscous dissipation. This model spectrum is illustrated on Figure 1.

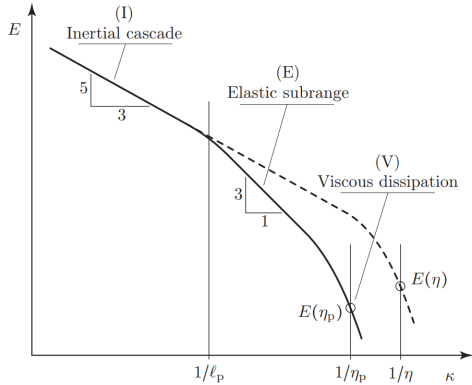


Figure 1: Model spectrum for turbulence in polymer solutions indicating three regions. From [6].

The (I) Inertial cascade on Figure 1 consists on a Newtonian inertial cascade at low wavenumbers.

According to [6], the (E) Elastic subrange is a spectral region separated from the inertial cascade by the Lumley scale  $l_p$ , which is determined by the elastic properties of the fluid and the turbulence dissipation rate. In this region, fractions of the turbulence kinetic energy arriving from the inertial subrange are converted into elastic energy by polymer stretching. Subsequent relaxation of the stretched polymers dissipates a part of this elastic energy due to the viscous drag of the polymer molecules in the solvent and interactions between monomers of a single polymer. The remaining elastic energy is transformed back to turbulence kinetic energy. Consequently, the energy flux on this region is continuously reduced from higher to lower wavenumbers.

Experimental data [6] suggested that this region follows a power-law with a slope of  $-3$ , where the polymer stresses overcome the viscous stresses. The energy spectrum in a turbulent structure of wavenumber  $k$  decreases according to:

$$E(k) = C_k \epsilon_0^{2/3} l_p^{5/3} (l_p k)^{-3} \quad (1)$$

where  $\epsilon_0$  is equal to the energy flux from the Newtonian inertial cascade.

The (V) Viscous subrange consists on a region dominated by viscous stresses which transform turbulence kinetic energy into heat, similarly to the dissipation range in the Newtonian spectrum.

### 2.1. Turbulent Planar Jets

The turbulent plane jet flow is a type of flow belonging to the free shear flow type, which are characterised by developing far away from the interaction with boundaries, and that advances along a preferred direction.

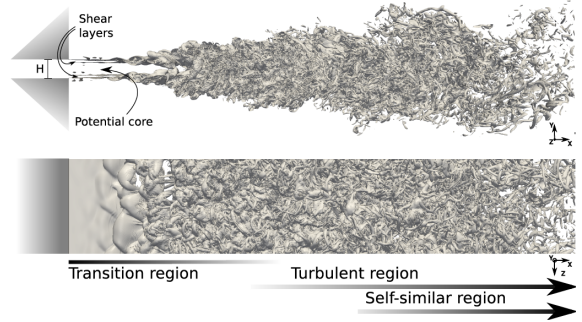


Figure 2: Turbulent planar jet regions. From [7].

This type of flow is characterised by being statistically two-dimensional, with a dominant direction of mean flow across the streamwise  $x$  direction and a mean velocity in the spanwise  $z$  direction of zero. The plane jet can be split across different regions: the potential core region near the jet inlet, originated by the high velocity gradient between the flow incoming from the jet inlet and that of the remaining environment; the transition region which comprises the area in which the flow experiences transition into a fully developed turbulent state; and the self-similarity region, in which the flow characteristics can be collapsed seamlessly after being properly scaled following the Kolmogorov's hypothesis.

### 2.2. Turbulence in dilute polymer solutions: numerical simulations

To model the polymer in numerical computations, the FENE-P model is the most widely used. The polymer orientation is represented as a continuous second-order tensor field, the so-called conformation tensor. This is defined as the normalised second moment of the end-to-end vector between the two beads [8], described as:

$$C_{ij} = \frac{\langle r_i r_j \rangle}{\frac{1}{3} \langle r^2 \rangle_{eq}} \quad (2)$$

where  $r_i$  is the instantaneous orientation of a polymer dumbbell,  $r_{eq}^2$  is the square of the equilibrium separation distance, and the angle brackets imply an ensemble average over the configuration space of the dumbbell.

The conformation tensor  $C_{ij}$  is a symmetric and positive definite (SPD) matrix. While mathematically this constraint is satisfied by the governing equations, these properties can be lost due to cumulative numerical errors. Several attempts at numerical simulation of visco-elastic turbulence were plagued by Hadamard instabilities, loss of conservation or over dissipation [9]. A recent approach has overcome these shortcomings [8], consisting on an algorithm based on the method of Kurganov and Tadmor (KT). This second-order scheme guaran-

tees that a positive scalar will remain so at all points and it was generalized to guarantee that a SPD tensor also remains SPD. Furthermore, the method dissipates less elastic energy than methods based on artificial diffusion, resulting in stronger polymerflow interactions.

### 3. Governing equations and Numerical Methods

It is important to note that the starting point of the numeric work here presented is a DNS code for turbulent jet described in [7, 10]. Both thesis were concerned about DNS of Newtonian fluids, presenting extensive validation of the DNS of turbulent jets. The main added features were the introduction of the Conformation tensor transport equation, the coupling of the Navier-Stokes momentum equation with the Polymer Stress Tensor and the use of ghost cells data on streamwise slab configuration.

#### 3.1. Velocity Field

On the velocity field governing equations, it is assumed that the fluid is incompressible and that it satisfies the continuity and momentum equations with an additional term related with divergence of polymer stress.

$$\frac{\partial u_i}{\partial x_i} = 0 \quad (3)$$

$$\frac{\partial u_i}{\partial t} + u_k \frac{\partial u_i}{\partial x_k} = -\frac{1}{\rho} \frac{\partial p}{\partial x_i} + \frac{1}{\rho} \frac{\partial T_{ij}}{\partial x_j} \quad (4)$$

where  $u_i$  is the  $i$  component of the velocity vector,  $\rho$  is the constant fluid density,  $p$  is the local pressure and  $T_{ij}$  is the combination of the viscous and polymer stress tensors. The latter can be expressed as a linear sum of contributions from the Newtonian stress ( $T_{ij}^{[s]}$ ) and the polymer stress ( $T_{ij}^{[p]}$ ):

$$T_{ij} = T_{ij}^{[s]} + T_{ij}^{[p]} \quad (5)$$

where the Newtonian stress  $T_{ij}^{[s]}$  is given by:

$$T_{ij}^{[s]} = 2\nu^{[s]} \frac{\partial S_{ij}}{\partial x_j} \quad (6)$$

being  $\nu^{[s]}$  the kinematic viscosity of the fluid. The  $S_{ij}$  is the Strain Rate Tensor defined as:

$$S_{ij} = \frac{1}{2} \left( \frac{\partial u_i}{\partial x_j} + \frac{\partial u_j}{\partial x_i} \right) \quad (7)$$

#### 3.2. The FENE-P Constitutive Model

FENE-P model constitutive equation of the Polymer Stress Tensor yields the following relationship:

$$T_{ij}^{[p]} = \frac{\rho\nu^{[p]}}{\tau_p} [f(C_{kk})C_{ij} - \delta_{ij}] \quad (8)$$

where  $C_{ij}$  is the conformation tensor,  $\nu^{[p]}$  the zero shear-rate polymeric viscosity,  $\delta_{ij}$  is the Kronecker

delta,  $L$  is the maximum possible extension of polymers and  $\tau_p$  is the Zimm relaxation time of the polymer. The polymer viscosity  $\nu^{[p]}$  is included in the model by a non-dimensional parameter  $\beta$ , which represents the ratio between the solvent and the zero-shear-rate viscosity:

$$\beta = \frac{\nu^{[s]}}{\nu^{[p]} + \nu^{[s]}} \quad (9)$$

The function  $f(C_{kk})$  is the Peterlin function given by:

$$f(C_{kk}) \equiv \frac{L^2 - 3}{L^2 - C_{kk}} \quad (10)$$

where  $C_{kk} = C_{xx} + C_{yy} + C_{zz}$  is the trace of the conformation tensor, which represents the extension length. This function ensures finite extensibility, as it gives rise to a non-linear spring force that diverges as  $\sqrt{C_{kk}} \rightarrow L$ , preventing the spring from extending beyond  $L$  [8].

To complement the continuity equation and the conservation of momentum equation, a transport equation for the conformation tensor  $C_{ij}$  is required. The conformation tensor evolution equation is given by:

$$\frac{\partial C_{ij}}{\partial t} + u_k \frac{\partial C_{ij}}{\partial x_k} = \frac{\partial u_i}{\partial x_k} C_{jk} + \frac{\partial u_j}{\partial x_k} C_{ik} - \frac{1}{\rho} \frac{T_{ij}^{[p]}}{\nu^{[p]}} \quad (11)$$

The former equation is solved simultaneously with the velocity field flow equations, ensuring polymer-flow interaction as the polymer molecules are deformed by the velocity field and, in turn, the resulting conformation tensor introduces a polymeric stress on the flow structure.

#### 3.3. Computational domain

The computational domain for the turbulent jet spatial simulation consists of a box with uniform grid and with  $L_x, L_y$  and  $L_z$  dimensions in each of the  $x$  (streamwise),  $y$  (normal) and  $z$  (spanwise) directions (see Figure 3). The  $y$  and  $z$  directions have periodic boundary conditions, whilst the streamwise  $x$  is a non-periodic direction with inflow and outflow boundaries.

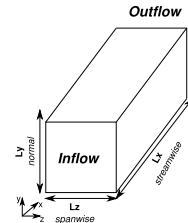


Figure 3: View of the computational domain with reference frame and notation. From [7].

### 3.4. Numerical scheme

The code employs the following structure: Momentum equation terms highly accurate pseudo-spectral schemes to solve derivative on the normal and spanwise directions, and uses a compact scheme on the streamwise direction. As for the Conformation Tensor Transport equation, it is employed the 2<sup>nd</sup> order scheme Kurganov-Tadmor and finite difference method.

The spatial discretization for the momentum equation is presented with detail on [10].

The Conformation Tensor Transport equation convection term is discretized with a second-order KT scheme, described in [8]. Spatial derivatives are second-order accurate everywhere, except for the grid points losing SPD property. Where it occurs the scheme automatically reverts to first-order accurate for that grid point to maintain the SPD property is maintained. This scheme is given by:

$$\mathbf{u} \cdot \nabla \mathbf{C} = \frac{\mathbf{H}_{i+1/2,j,k}^x - \mathbf{H}_{i-1/2,j,k}^x}{\Delta x} + \frac{\mathbf{H}_{i,j+1/2,k}^y - \mathbf{H}_{i,j-1/2,k}^y}{\Delta y} + \frac{\mathbf{H}_{i,j,k+1/2}^z - \mathbf{H}_{i,j,k-1/2}^z}{\Delta z} \quad (12)$$

where the convective flux tensor  $\mathbf{H}$  in each direction is given by:

$$\mathbf{H}_{i+1/2,j,k}^x = \frac{1}{2} u_{i+1/2,j,k} (\mathbf{C}_{i+1/2,j,k}^+ + \mathbf{C}_{i+1/2,j,k}^-) - \frac{1}{2} |u_{i+1/2,j,k}| (\mathbf{C}_{i+1/2,j,k}^+ - \mathbf{C}_{i+1/2,j,k}^-) \quad (13)$$

$$\mathbf{H}_{i,j+1/2,k}^y = \frac{1}{2} v_{i,j+1/2,k} (\mathbf{C}_{i,j+1/2,k}^+ + \mathbf{C}_{i,j+1/2,k}^-) - \frac{1}{2} |v_{i,j+1/2,k}| (\mathbf{C}_{i,j+1/2,k}^+ - \mathbf{C}_{i,j+1/2,k}^-) \quad (14)$$

$$\mathbf{H}_{i,j,k+1/2}^z = \frac{1}{2} w_{i,j,k+1/2} (\mathbf{C}_{i,j,k+1/2}^+ + \mathbf{C}_{i,j,k+1/2}^-) - \frac{1}{2} |w_{i,j,k+1/2}| (\mathbf{C}_{i,j,k+1/2}^+ - \mathbf{C}_{i,j,k+1/2}^-) \quad (15)$$

The conformation tensor  $\mathbf{C}$  at the interface is constructed from the following second-order linear approximations:

$$\mathbf{C}_{i+1/2,j,k}^\pm = \mathbf{C}_{i+1/2\pm 1/2,j,k} \mp \left( \frac{\Delta x}{2} \right) \left( \frac{\partial \mathbf{C}}{\partial x} \right)_{i+1/2\pm 1/2,j,k} \quad (16)$$

$$\mathbf{C}_{i,j+1/2,k}^\pm = \mathbf{C}_{i,j+1/2\pm 1/2,k} \mp \left( \frac{\Delta y}{2} \right) \left( \frac{\partial \mathbf{C}}{\partial y} \right)_{i,j+1/2\pm 1/2,k} \quad (17)$$

$$\mathbf{C}_{i,j,k+1/2}^\pm = \mathbf{C}_{i,j,k+1/2\pm 1/2} \mp \left( \frac{\Delta z}{2} \right) \left( \frac{\partial \mathbf{C}}{\partial z} \right)_{i,j,k+1/2\pm 1/2} \quad (18)$$

The spatial derivatives of the conformation tensor are:

$$\left( \frac{\partial \mathbf{C}}{\partial x} \right)_{i,j,k} = \begin{cases} \frac{\mathbf{C}_{i+1,j,k} - \mathbf{C}_{i,j,k}}{\Delta x} \\ \frac{\mathbf{C}_{i,j,k} - \mathbf{C}_{i-1,j,k}}{\Delta x} \\ \frac{\mathbf{C}_{i+1,j,k} - \mathbf{C}_{i-1,j,k}}{2\Delta x} \end{cases} \quad (19)$$

It is selected the derivative approximation that can yield SPD results for  $\mathbf{C}_{i-1/2}^+$  and  $\mathbf{C}_{i+1/2}^-$ . When two or more candidates satisfy the criterion, it is selected the one which maximizes the minimum eigenvalue for these two tensors. When none of them meet this criterion, the derivative is set to zero, reducing to first-order accurate. This slope limiting procedure will ensure that all  $\mathbf{C}^\pm$  are SPD.

The update of the conformation tensor  $\mathbf{C}$  requires the area-averaged velocity at the edge of the volume surrounding each grid point. In [8], the velocities  $u(x, y, z)$ ,  $v(x, y, z)$  and  $w(x, y, z)$  are obtained from the inverse transform of the Fourier coefficients  $\hat{u}(k_x, k_y, k_z)$ ,  $\hat{v}(k_x, k_y, k_z)$  and  $\hat{w}(k_x, k_y, k_z)$ . However, since the streamwise direction  $x$  is not periodic this method is not applicable. Thus, the area-averaged velocities are computed considering the physical domain along the streamwise direction  $x$  and in the spectral domain along the normal  $y$  and spanwise  $z$  directions. The resulting expressions for the cell velocities are:

$$u_{i+1/2,j,k} = FT^{-1} \left\{ \hat{u}(x, k_y, k_z) \frac{\sin(k_y \frac{\Delta y}{2})}{k_y \frac{\Delta y}{2}} \frac{\sin(k_z \frac{\Delta z}{2})}{k_z \frac{\Delta z}{2}} \right\} \quad (20)$$

$$v_{i,j+1/2,k} = \frac{1}{\Delta x} \int_{x_i - \frac{\Delta x}{2}}^{x_i + \frac{\Delta x}{2}} \left\{ \hat{v}(x, k_y, k_z) e^{ik_y \frac{\Delta y}{2}} \frac{\sin(k_z \frac{\Delta z}{2})}{k_z \frac{\Delta z}{2}} \right\} dx \quad (21)$$

$$w_{i,j,k+1/2} = \frac{1}{\Delta x} \int_{x_i - \frac{\Delta x}{2}}^{x_i + \frac{\Delta x}{2}} \left\{ \hat{w}(x, k_y, k_z) e^{ik_z \frac{\Delta z}{2}} \frac{\sin(k_y \frac{\Delta y}{2})}{k_y \frac{\Delta y}{2}} \right\} dx \quad (22)$$

where  $FT^{-1}$  is the inverse fast Fourier transform,  $\hat{u}(x, k_y, k_z)$ ,  $\hat{v}(x, k_y, k_z)$  and  $\hat{w}(x, k_y, k_z)$  are the Fourier coefficients at each grid point. For the streamwise direction it is required to calculate the velocity and integrate along  $x$  in the physical space. Along the streamwise direction  $x$ , the velocity on the cell edge is interpolated with 5<sup>th</sup> order Lagrange Polynomials and the integration along

the streamwise direction is performed considering Gauss-Legendre 3 point rule. The area averaged velocity for  $v$  component is then the following:

$$v(i, j + 1/2, k) = \frac{1}{2} \left[ A_i F \left( x + \frac{\Delta x}{2} \xi_i \right) \right] \quad (23)$$

$$F(x) = FT^{-1} \left\{ \hat{v}(x, k_y, k_z) e^{ik_y \frac{\Delta y}{2}} \frac{\sin(k_z \frac{\Delta z}{2})}{k_z \frac{\Delta z}{2}} \right\} \quad (24)$$

where  $\xi_i$  and  $A_i$  are the Gauss nodes and weights, respectively. The area averaged spanwise velocity  $w$  is obtained analogously to  $v$ .

It should be noted that the formulation presented is applicable to the velocity on positive edges  $i+1/2$ ,  $j+1/2$  and  $k+1/2$ . The area averaged velocities on negative edges  $i-1/2$ ,  $j-1/2$  and  $k-1/2$  are obtained by shifting one position backwards the positive edge velocity field in the respective velocity direction. This shifting requires special treatment on the boundaries. For the normal  $v$  and spanwise  $w$  velocities, the lower boundary for the negative edge cell velocities is equal to the upper boundary positive edge cell velocities, thus ensuring a period behaviour. Regarding the streamwise velocity  $u$ , the negative cell edge velocity at the inlet boundary is assumed to be the velocity  $u$  at the inlet.

The Conformation Tensor Transport equation stretching term is computed with a central difference scheme second-order accurate everywhere in space, except for the boundaries on the streamwise direction. This scheme results in:

$$\frac{\partial u_i}{\partial x_k} C_{jk} + \frac{\partial u_j}{\partial x_k} C_{ik} = \frac{(u_i)_{m+1} - (u_i)_{m-1}}{2\Delta x_k} C_{jk} + \frac{(u_j)_{m+1} - (u_j)_{m-1}}{2\Delta x_k} C_{ik} \quad (25)$$

where  $i$ ,  $j$  and  $k$  are the computational indexes and  $m$  is an auxiliary variable that represents  $i$ ,  $j$  and  $k$  for the  $\partial/\partial x$ ,  $\partial/\partial y$  and  $\partial/\partial z$  derivatives, respectively. On the inlet and outlet boundaries the central difference scheme is reverted to a forward and backward finite difference first-order accurate scheme, respectively. The polymer stress coupling term on the momentum equations also considers a central difference scheme second-order accurate, reverting to first-order accurate on the inlet and outlet boundaries.

The time advancement method of the momentum equation and for the conformation tensor transport equation is an explicit  $3^{rd}$  order Runge-Kutta scheme of numerical integration.

### 3.5. Boundary and Initial Conditions

The velocity profile imposed at the inlet at each timestep is given by:

$$u(x_0, t) = U_{med}(x_0) + U_{noise} \quad (26)$$

where  $x_0$  is the inlet plane,  $U_{noise}$  is a superimposed random numerical noise and  $U_{med}$  is the mean inlet profile given by:

$$U_{med}(x_0) = \frac{U_2 + U_1}{2} + \frac{U_2 - U_1}{2} \tanh \left[ \frac{h}{4\theta_0} \left( 1 - \frac{2|y|}{h} \right) \right] \quad (27)$$

In (27)  $\theta_0$  is the momentum thickness of the initial shear layer,  $h$  is the jet inlet slot width and  $y$  is the distance from the centre of the jet.  $U_1$  is the co-flow velocity and  $U_2$  is the centreline velocity. The co-flow is required to allow the growth of the jet's shear layer, otherwise hampered by the lack of natural entrainment from the periodic lateral boundaries.

The numerical noise,  $U_{noise}$ , is superposed to the mean profile in (27), at each timestep  $t$  by imposing a three-component fluctuating velocity field ( $u$ ,  $v$  and  $w$ ), in order to exhibit the statistical characteristics of isotropic turbulence [11].

The inlet boundary for the polymer conformation tensor is imposed at each timestep and is based on the assumption of steady flow, fully developed in the streamwise direction  $x$ . Considering the inlet velocity profile without co-flow (see equation (27)), one obtains an analytical profile for the polymer conformation tensor, given by the real root of the following cubic equation:

$$C_{22}^3 + \frac{L^2}{2\tau_p^2 \left( \frac{\partial U}{\partial y} \right)^2} C_{22} - \frac{L^2}{2\tau_p^2 \left( \frac{\partial U}{\partial y} \right)^2} = 0 \quad (28)$$

The lateral boundaries are periodic, which requires this periodicity to be stated for all three components of the velocity field, the pressure and the polymer conformation tensor. For a given quantity  $\phi(x, y, z, t)$  these are given by:

$$\begin{aligned} \phi(x, y, z, t) &= \phi(x, y + L_y, z, t) \\ \phi(x, y, z, t) &= \phi(x, y, z + L_z, t) \end{aligned} \quad (29)$$

The outlet boundary is the most sensitive boundary condition of the planar jet. The fluid structures that leave the domain must exit unperturbed by the outflow condition and ensuring that reflected waves do not go back into the domain. Therefore, the code employs a non-reflective boundary condition used by [12], where all the terms of the Navier-Stokes equations are explicitly advanced.

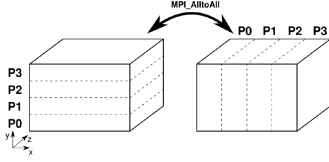


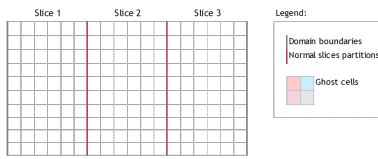
Figure 4: View of the domain partitioning with reference frame and notation. From [10].

### 3.6. Code architecture

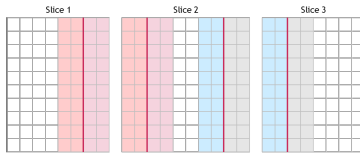
The computational domain is implemented on a mixed decomposition, with the co-existence of streamwise slabs and normal slices (see Figure 4).

The data field configuration is swapped according to the operation taking place. The direct and inverse Fourier transforms are computed in independent  $yz$  planes, thus being intrinsically connected to the normal slice configuration. The compact scheme for the streamwise derivatives is computed on the slab configuration, as it requires a complete line of data on the streamwise direction not available on normal slice configuration. The streamwise derivatives for the conformation tensor transport equation do not require complete lines of data on the streamwise  $x$  direction. Thus, it was opted to perform the calculation on the normal slice configuration with the aid of ghost cells, avoiding the need to perform intensive communications between processors to swap data configuration.

Ghost cells here consist in replicated data from neighbouring partitions that is passed between processors. This process requires data exchange at each Runge-Kutta sub-step. An illustrative example of ghost cell application is presented in Figure 5.



(a) Normal slice configuration without ghost cell data on the  $xy$  plane.



(b) Normal slice configuration with ghost cell data on the  $xy$  plane.

Figure 5: Ghost cell configuration data exchange on the streamwise direction for a domain partitioned in 3 normal slices.

## 4. Code Verification

The Conformation Tensor Transport Equation was verified with a frozen in time 2D Couette flow, thus allowing the comparison with a steady analytical solution. The velocity profile (see Figure 6) was kept constant throughout the simulation by imposing it in each Runge-Kutta step.

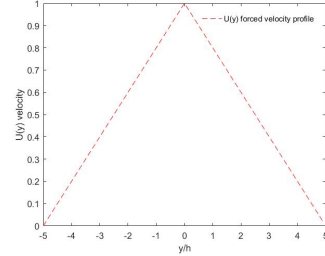


Figure 6:  $u$  velocity profile in the  $y$  direction.

From Figure 6 it is noticeable that the velocity profile is a mirrored Couette profile, due to the numerical scheme and the need to ensure periodic conditions. Therefore, the discontinuity points observed on the profile ( $y/h = -5, 0, 5$  for Figure 6) are not comparable to the analytical solution.

The conformation tensor  $C_{ij}$  is a SPD matrix by definition. For this reason,  $C_{ij} = C_{ji}$  and, therefore, the system of linear equations only encompasses six independent variables.

As it is considered a steady and fully-developed flow in the streamwise  $x$  direction, the following assumptions are enforced:

$$\frac{\partial}{\partial t} = 0, \quad \frac{\partial}{\partial x} = 0 \quad (30)$$

Given the two-dimensional flow (velocity profile  $u(y)$ ) and the conservation of mass, it follows:

$$v = 0, w = 0, \quad \frac{\partial}{\partial z} = 0 \quad (31)$$

Considering the flow assumptions from Equations (30) and (31), the conformation tensor transport equation (11) can be rewritten in this case as:

$$u_k \frac{\partial C_{ij}}{\partial x_k} = \frac{\partial u_i}{\partial x_k} C_{jk} + \frac{\partial u_j}{\partial x_k} C_{ik} - \frac{1}{\tau_p} [f(C_{kk})C_{ij} - \delta_{ij}] \quad (32)$$

Having equation (32), each entry of the conformation tensor can be organized as a function of  $C_{22}$ . The solution for  $C_{22}$  can be obtained from the cubic polynomial described in equation (28), for which

the real root solution is:

$$C_{22} = \sqrt[3]{\frac{L^2}{4\left(\frac{\partial u}{\partial y}\right)^2 \tau_p^2} + \sqrt{\frac{L^6}{216\left(\frac{\partial u}{\partial y}\right)^6 \tau_p^6} + \frac{L^4}{16\left(\frac{\partial u}{\partial y}\right)^4 \tau_p^4}} + \sqrt[3]{\frac{L^2}{4\left(\frac{\partial u}{\partial y}\right)^2 \tau_p^2} - \sqrt{\frac{L^6}{216\left(\frac{\partial u}{\partial y}\right)^6 \tau_p^6} + \frac{L^4}{16\left(\frac{\partial u}{\partial y}\right)^4 \tau_p^4}}} \quad (33)$$

The followings simulation parameters were considered on the verification exercise:

Box height $h$	$2\pi$
Box dimensions (terms of $h$ )	$0.9 \times 1 \times 0.118$
Mesh	$128 \times 128 \times 128$
Max. velocity $u_{max}$	1
Zero shear-rate viscosity $\nu^{[p]}$	0.002
Max. molecular extensibility $L$	10
Relaxation time (s) $\tau_p$	0.1
Polymer concentration $\beta$	0.8

Table 1: Verification simulation parameters.

Having both analytical and numerical results, it is performed the comparison between both. This verification is presented in Figures 7 and 8 for the diagonal and non-diagonal conformation tensor components, respectively. In each figure the dashed lines correspond to the numerical solution, whilst the solid lines refer to the analytical solution.

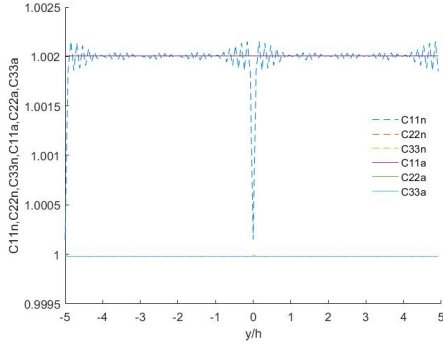


Figure 7: Numerical (n) and analytical (a) solutions for  $C_{ii}$  considering a  $u$  velocity profile in the  $y$  direction.

From Figures 7 and 8 it is possible to observe that the numerical and analytical solutions present the same results, thus ensuring the verification of the triggered equation components. For the remaining scenarios the same conclusion is obtained.

## 5. Results

Several runs were performed in order to study the influence of polymer additives on the turbulent pla-

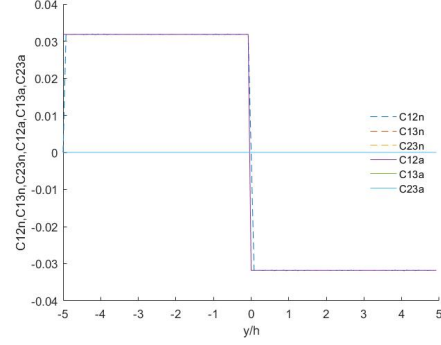


Figure 8: Numerical (n) and analytical (a) solutions for  $C_{ij}$ ,  $i \neq j$  considering a  $u$  velocity profile in the  $y$  direction.

nar jet. It should be noted that the results were produced as part of an ongoing investigation with Mateus C. Guimaraes [13], considering the numerical algorithm developed in this work. The computational and physical parameters of the runs are presented in Tables 2 and 3.

$n_x$	$n_y$	$n_z$	$L_x/h$	$L_y/h$	$L_z/h$
512	512	128	18	18	4

Table 2: Computational domain parameters for the simulations. Number of grid points ( $n_x, n_y, n_z$ ); non-dimensional grid size ( $L_x/h, L_y/h, L_z/h$ ).

The  $W_i$  is given by the ratio between the polymer relaxation time and Kolmogorov time scale:

$$W_i = \frac{\tau_p}{\tau_s} \quad (34)$$

where  $\tau_s$  represents the Kolmogorov time scale ( $\tau_s = (\nu^{[s]}/\epsilon^{[s]})^{(1/2)}$ ). The Reynolds number based on the Taylor microscale is defined as:

$$Re_\lambda = \frac{u'\lambda}{\nu^{[s]}} \quad (35)$$

where  $u'$  is the reference perturbation velocity and  $\lambda$  is the Taylor scale. The Taylor scale  $\lambda$  is given by the viscous dissipation rate assuming local isotropy at the jet centreline:

$$\lambda = \sqrt{\frac{15\nu^{[s]} \bar{u}'^2}{\epsilon^{[s]}}} \quad (36)$$

In order to simulate the smallest scales that are present in the flow, the grid size has to be of the order of the Kolmogorov scale  $\eta$ , defined in terms of the solvent turbulent viscous energy dissipation rate  $\epsilon^{[s]}$  and the solvent viscosity  $\nu^{[s]}$ :

$$\eta = \left( \left( \nu^{[s]} \right)^3 / \epsilon^{[s]} \right)^{1/4} \quad (37)$$

Case	$W_i$	$Re$	$Re_\lambda$	$\tau_p(s)$	$\beta$	$\Delta x/\eta_{14h}$
A	0	3500	100	0	1	4.0
B	0.33	3500	110	0.025	0.8	4.0
C	0.65	3500	110	0.05	0.8	4.0
D	1.19	3500	110	0.10	0.8	3.9
E	1.66	3500	140	0.20	0.8	3.4
F	0.20	3500	120	0.025	0.6	3.8
G	0.27	3500	160	0.20	0.6	3.3
H	1.35	3500	160	0.025	0.4	3.3
I	1.55	3500	180	0.20	0.4	3.1
J	2	3500	200	0.40	0.8	2.8
K	2.6	3500	220	0.60	0.8	2.5
L	3.3	3500	250	0.80	0.8	2.3

Table 3: Physical parameters for the simulations. Weissenberg number  $W_i$ ; slot width, initial maximum jets velocity, solvent viscosity based Reynolds number  $Re$ ; Averaged Taylor turbulence micro-scale centreline velocity solvent viscosity based Reynolds number on the  $x$  direction  $Re_\lambda$ ; polymer relaxation time  $\tau_p$ ; polymer concentration  $\beta$ ; mesh resolution normalized by the Kolmogorov small scale at  $x/h = 14$ . Polymer normalized maximum extensibility  $L$  of 100 for all cases.

According to [10], several authors state that the ratio of the element size  $\Delta x$  to the Kolmogorov scale  $\eta$  should have a value of the order of 2.0 to 3.0. It was opted to select to analyse  $\Delta x/\eta$  at  $x/h = 14$ , as this region refers to a fully developed turbulent region of the jet. By having mesh resolution normalized by the Kolmogorov small scales within the literature values, the mesh size was deemed adequate.

The simulations are started with variable time step and constant Courant number ( $CFL = 1/6$ ). Once self-similarity is attained, the time step is kept constant at a lower level than the minimum reached during the first part of the simulation and statistical quantities are computed by accumulating data.

The half-width or mean flow thickness  $\delta$  is defined as follows according to [13]:

$$\delta = \int_0^\infty \frac{\bar{u} - U_{2L}}{U_c - U_{2L}} dy \quad (38)$$

where  $U_c$  is the centreline velocity and  $U_{2L}$  is the local co-flow velocity. The streamwise velocity is non-dimensionalized according to the following expression:

$$\left( \frac{U_1 - U_2}{\langle U_c \rangle - U_2} \right)^2 \quad (39)$$

where  $U_1$  is the inlet centreline velocity and  $U_2$  is the inlet co-flow velocity.

All variables presented in this section are an average on time and on the  $z$  spanwise direction.

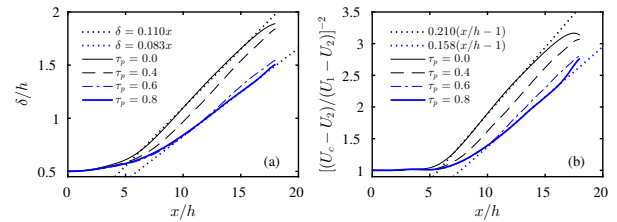


Figure 9: Streamwise evolution of non-dimensional (a) jet's half-width and (b) centreline velocity for cases A, J, K and L. From [13].

On Figure 9 it is possible to identify the self-similar region by fitting straight lines to the linear region of each curve. A good linear fit was found between  $x/h = 6$  to  $x/h = 17$  for the Newtonian case, whilst for the case with  $\tau_p = 0.8$  a good linear fit was observed from  $x/h = 10$  to  $x/h = 17$ .

From Figure 9 (a) it is noticeable a lower jet width on the visco-elastic cases in comparison to the Newtonian case. Similarly, the centreline velocity shows a larger value on the visco-elastic cases than on the Newtonian case. Both these remarks are indicative of a lower energy dissipation rate for the FENE-P solutions due to the interaction of the polymer particles on the flow physics. This result follows the expected trend, as polymer particles are expected to absorb elastic energy at a higher rate from the flow, reducing the overall energy dissipation of the flow.

On Figure 10 it is shown statistical quantities for a fully turbulent streamwise cross-section ( $x/h = 12$ ). It is possible to observe that the streamwise  $u$  velocity profiles collapse for different relaxation time. Concerning the normal  $y$  velocity profile, it is noted that a higher polymer relaxation time leads to, typically, a lower average normal velocity magnitude. The spanwise  $w$  average velocity is not presented, since it presents an average zero value for a planar jet [10]. As for the velocity perturbation root mean squared components, it is observed an overall decrease of all components with increasing polymer relaxation time. Moreover, it is seen that all perturbation velocities converge to zero with higher distances from the centreline, as the flow is moving towards zones not perturbed by the jet. Concerning the Reynolds shear stresses, the examination of Figure 10 indicates that for higher polymer relaxation time the shear stress reduces, namely for cases K and L. This observation reinforces the previous remark, indicating a smaller energy dissipation rate for the polymer solution case due to the energy-absorption effect of the polymers.

The conformation tensor  $C_{ij}$  are plotted for the

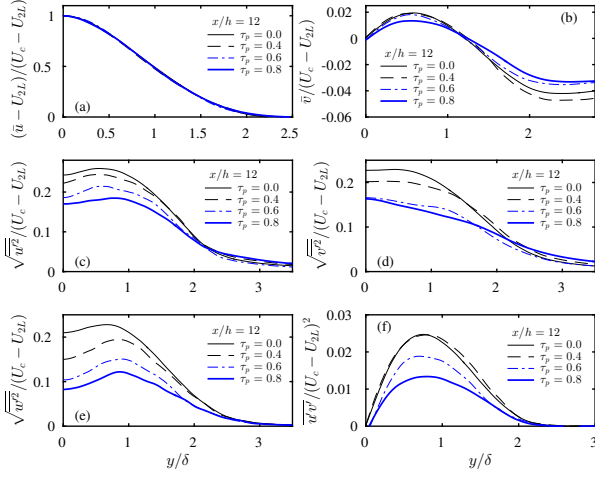


Figure 10: Normalized mean velocity: (a) streamwise and (b) normal direction, (c-e) velocity root mean squared components and (f) Reynolds shear stress profiles for cases A, J, K and L. From [13].

same streamwise cross-section ( $x/h = 12$ ) in Figure 11. The averaged conformation tensor components  $C_{13}$  and  $C_{23}$  are not presented in Figure 11, as due to the nature of the turbulent flow it is possible to prove that the average value of these components is zero. This was observed on the simulation results. Concerning the remaining conformation tensor components, it is seen that with increasing polymer relaxation time, the magnitude of the averaged  $C_{ij}$  increases. Moreover, one notices that the average values converges to the polymer equilibrium state, that is value 1 for the diagonal tensor terms and 0 for the remaining tensor terms, on the non-perturbed region of the flow. As the elastic energy stored by a stretched polymer is proportional to the trace of the conformation tensor, the observed higher average values of the conformation tensor components with increasing polymer relaxation time indicate that the polymer molecules have an increasing absorbed elastic energy.

On Figure 12 it is presented the Weissenberg number for the  $y = 0$  cross-section. It is observed that for higher polymer relaxation time with the same  $\beta$  (especially clear on cases with  $\beta = 0.8$ ),  $W_i$  number increases. Simultaneously, the same cases when viewed from a turbulent kinetic energy dissipation perspective (see Figure 13) present a lower viscous energy dissipation, which in turn would contribute to a lower  $W_i$  number. Thus, this indicates that the polymer elastic forces on the flow are far more significant than the solvent viscous forces.

If one considers cases with an equal  $\tau_p$  (e.g.  $\tau_p = 0.2s$ ), it is noticeable that higher  $\beta$  leads to a higher  $W_i$  number. Nonetheless, the variation on the Weissenberg number is clearly smaller with the influence

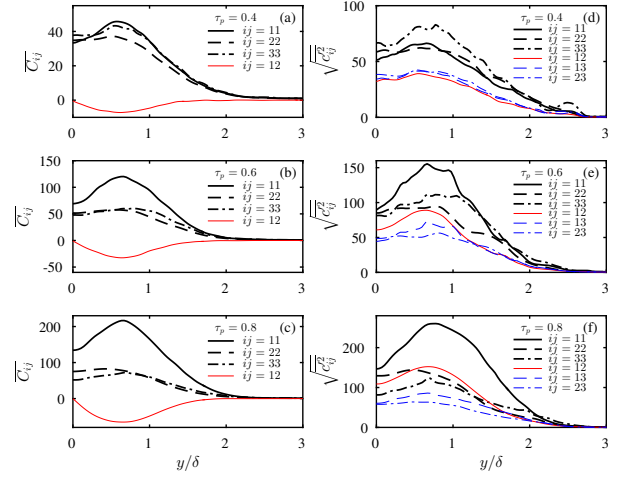


Figure 11: Mean (a-c) and root mean squared (d-f) components of the conformation tensor at  $x/h = 12$  for cases J, K and L. From [13].

of  $\beta$  than with the influence of  $\tau_p$ .

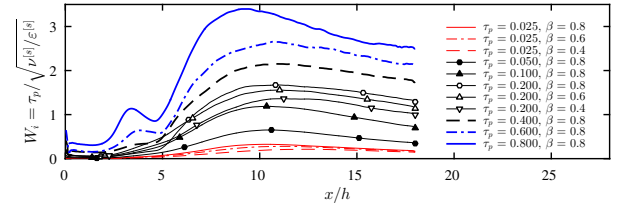


Figure 12: Streamwise evolution of centreline Weissenberg number for visco-elastic cases. From [13].

As for the viscous energy dissipation rate presented in Figure 13, it is noted that the presence of polymer additives on the flow leads to a lower viscous energy dissipation rate. Moreover, for the same  $\tau_p$  a lower  $\beta$  leads to lower viscous energy dissipation. Similarly, for the same  $\beta$  a higher  $\tau_p$  leads to lower viscous energy dissipation.

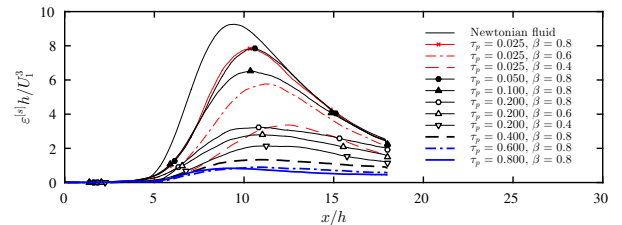


Figure 13: Streamwise evolution of centreline turbulent kinetic energy dissipation of the solvent for all cases. From [13].

## 6. Conclusions

In the present work it was implemented the FENE-P model within an existing DNS tool, resulting in

a DNS tool for turbulent spatial jet with polymer additives. It is important to stress that DNS or experimental analyses of turbulent spatial jet have not been found in the literature. As such, this work provides the first time a turbulent spatial jet is analysed with a FENE-P visco-elastic configuration, leading to a new ground breaking numerical tool with potential for new study areas.

During the development of the current work, extensive care was taken concerning the numerical implementation in order to ensure impact minimization of the implementation of FENE-P on the overall DNS code performance. Such was achieved with the inclusion of the ghost cells mechanism and minimization of the call of MPI commands, which allowed a relevant performance enhancement. Iteration times with FENE-P on the spatial jet code resulted in an increase of 7-fold, whilst for comparable homogeneous isotropic turbulent FENE-P simulations a 10-fold increase was observed.

DNS analyses were performed, in which it was analysed the evolution of the jet's characteristics, the conformation tensor components evolution and the turbulent kinetic energy dissipation. Regarding the jet's characteristics, focus was given on the jet's width, velocity components and Reynolds shear stress profile. For all of the abovementioned, the difference between the Newtonian fluid and FENE-P solution is clear. The jet width in the FENE-P solution is lower than the one observed for the Newtonian case, which indicates that the viscous energy dissipation is smaller for the polymer solution case. Similarly, the centreline velocity shows a higher value for polymer solution than for the Newtonian case, confirming the previous remark. As for the remaining components, results show that velocity perturbations on turbulent regime are lower in the visco-elastic solution and that the Reynolds shear stress profiles decreases on the FENE-P solution. Both of the previous remarks confirm a smaller energy dissipation rate for the polymer solution case due to the energy-absorption effect of the polymers, which is indicative of the drag reduction phenomenon.

### Acknowledgements

Firstly, I would like to start thanking Professor Carlos Silva for giving me the opportunity to work in this area and for his advice during the thesis.

I would like to thank Mateus Guimaraes, for the data post-processing and obtaining the first results with the the algorithm developed within this work.

### References

[1] B. A. Toms. Some observations on the flow of linear polymers solutions through straight tubes at large reynolds numbers. In *Proc. 1st*

*Intern. Congr. Rheol.*, pages 135–141, North Holland, Amsterdam, 1948.

- [2] Karan Anand. *Numerical Heat Transfer Analysis of Micro-scale Jet-impingement Cooling in a High-pressure Turbine Vane*. PhD thesis, Ryerson University, 2011.
- [3] A.S. Dogonchi and D.D. Ganji. Investigation of heat transfer for cooling turbine disks with a non-newtonian fluid flow using dra. *Case Studies in Thermal Engineering*, 6:40–51, 2015.
- [4] A. Fouxon and V. Lebedev. Spectra of turbulence in dilute polymer solutions. *Physics of Fluids*, 15(7):2060–2072, 2003.
- [5] R. Jousot, S. Coumar, and V. Lago. Plasmas for high speed flow control. *Plasmas for Aeronautics*, 10(AL10-04), 2015.
- [6] Richard Vonlanthen. *The Effects of Fluid Elasticity on Grid Turbulence*. PhD thesis, cole Polytechnique Fdrale de Lausanne, Suisse, 2010.
- [7] R. N. Reis. *The dynamics of coherent vortices near the turbulent/non-turbulent interface analysed by direct numerical simulations*. PhD thesis, IST, Lisboa, 2011.
- [8] T. Vaithianathan, A. Robert, J. G. Brasseur, and L. R. Collins. An improved algorithm for simulating three-dimensional, viscoelastic turbulence. *J. Non-Newt. Fluid Mech.*, 140(1):3–22, 2006.
- [9] C. Laney. *Computational Gas Dynamics*. Cambridge University Press, 2000.
- [10] D. C. Lopes. *Direct and Large-Eddy Simulations of the Turbulent Entrainment of Passive Scalars in Planar Jets*. PhD thesis, IST, Lisboa, 2014.
- [11] C. B. da Silva and O. Mtais. On the influence of coherent structures upon interscale interactions in turbulent plane jets. *J. Fluid Mech.*, 473:103–145, 2002.
- [12] I. Orlanski. A simple boundary condition for unbounded hyperbolic flows. *Journal of Computational Physics*, 21(3):251–269, 1976.
- [13] Mateus C. Guimaraes. Report. Instituto Superior Tcnico, University of Lisbon, September 2018.